aerospace

MDPI

Article

Numerical Investigation on the Effect of Ammonium Perchlorate Content and Position on the Combustion Characteristics of an Ammonium Perchlorate/Hydroxyl-Terminated Polybutadiene Propellant

Di Sun [1,2], Yongzhou Li [2], Peijin Liu [1,*], Bofeng Chen [1] and Wei Fan [1]

[1] Science and Technology on Combustion, Internal Flow and Thermal-Structure Laboratory, Northwestern Polytechnical University, Xi'an 710072, China; sundi2004@126.com (D.S.); chenbf666@126.com (B.C.); weifan419@nwpu.edu.cn (W.F.)
[2] College of Aircraft Engineering, Nanchang Hangkong University, Nanchang 330063, China; nuaa2004@126.com
* Correspondence: liupj@nwpu.edu.cn

Abstract: A gas–solid-coupled sandwich combustion model was established for ammonium perchlorate (AP)/hydroxyl-terminated polybutadiene (HTPB) composite propellant. Numerical simulations were conducted to investigate the influence of the content of AP and the relative position of the coarse AP on the flame structure and the burning rate of the propellant. The results indicated that the overall AP mass fraction has a significant effect on the gas-phase flame temperature and burning rate, and there exists an optimal oxygen-to-fuel ratio that maximizes the burning rate. As the mass fraction of fine AP increased, the premixed flame above the binder matrix gradually took over the dominance of the diffusion flame, and the intensity of the diffusion flame near the interface of coarse AP and binder matrix also increased, resulting in a significant increase in the burning rate. As the mass fraction of fine AP increases from 0% to 70.0%, the average surface temperature increases from 937 K to 1026 K, and the burning rate rises from 0.9 cm/s to 2.7 cm/s. The location of the coarse AP causes the flame tilts to the side with less binder matrix, but it had little effect on the burn rate of the propellant.

Keywords: composite propellant; solid rocket motor; gas–solid-coupled model; flame structure; burning rate

Citation: Sun, D.; Li, Y.; Liu, P.; Chen, B.; Fan, W. Numerical Investigation on the Effect of Ammonium Perchlorate Content and Position on the Combustion Characteristics of an Ammonium Perchlorate/Hydroxyl-Terminated Polybutadiene Propellant. *Aerospace* **2023**, *10*, 692. https://doi.org/10.3390/aerospace10080692

Academic Editor: James 'Chris' Thomas

Received: 30 June 2023
Revised: 28 July 2023
Accepted: 1 August 2023
Published: 3 August 2023

1. Introduction

Solid rocket motors have been widely used as propulsion devices in missile weapons and rocket booster systems. Their performance is closely related to the combustion characteristics of the propellants [1,2]. The combustion of propellants is a complex, multidimensional physical and chemical process at high temperatures and pressure in solid rocket motors [3,4], which makes it difficult to observe and measure the parameters by experiment. In such cases, the use of numerical simulation based on combustion models is an effective method to study the flame structure and combustion mechanism.

As the most widely used propellant in the world [5–8], the AP/HTPB composite propellant has been studied by many researchers, and various steady-state combustion models based on experimental phenomena have been proposed to help understand the combustion processes and phenomena [9–12]. The Beckstead–Derr–Price (BDP) model is the most classic one, which describes the heating and combustion of AP and HTPB, including endothermic decomposition, condensed-phase surface reaction, solid-phase exothermic and gas-phase reaction, as well as the component transport process [13]. It assumes that there are three competitive flames, namely, the AP monopropellant flame, the primary diffusion flame, and the final diffusion flame. The one-dimensional model lays the foundation for the flame structure. Jeppson and Beckstead [14] found that the flame

properties vary with AP particle size. In light of this, a premixed composite flame produced by the combustion of fine AP and binder was suggested to be added to the multiple flame models. This reasonable improvement allows the BDP model to describe the burning process in more detail, and the flame structure has been observed by experiment [15,16]. However, as the diffusion combustion effect increases with an increasing AP particle diameter, the one-dimensional model restriction causes a significant difference between the calculated and experimental values of the burning rate.

Experimental observations have suggested that a composite solid propellant exhibits a quasi-periodic array at the mesoscale. It can be approximated as a sandwich propellant consisting of a series of parallel oxidizers and binders. While another random pack model is much closer to the real appearance of the composite propellant, its solid phase is too complex and requires the consumption of larger computational resources in the calculation process [17–19]. The sandwich model remains the simplest and most efficient one to study the mechanism of propellant combustion, preserving essential features of the heterogeneous propellant's multiphase material interface, simplifying the numerical modeling of its structure and mesh, and facilitating experimental observations and quantitative analysis. It has been widely used by many investigators in experiments and simulations.

Price et al. [20] conducted a study on factors affecting the combustion of sandwich propellants, including pressure, binder thickness, the thermal conductivity of interlayer material, and the presence of fine AP in the binder. Fitzgerald and Brewster [21] explored the flame-surface structure of sandwich propellants through experiments and numerical simulations and discovered that it is dependent on the scale, pressure, and equivalence-ratio disparity between no premixed fuel and oxidizer zones. Buckmaster et al. [22] applied the sandwich model to investigate the geometric structure of the diffusion flame created by propellant combustion. Hegab et al. [23] employed a sandwich combustion model to describe the non-planar burning surface regression of the AP/HTPB composite propellant and evaluated the impacts of different parameters on the stable propagation velocity. Gross and Beckstead [24] utilized the sandwich configuration and a detailed gas-phase kinetic mechanism diffusion flame model to analyze the flame structure of composite propellants and their sensitivity to AP particle size.

Although the simplification of the propellant into a sandwich structure has significantly improved the experimental observation of the flame profile, it is still challenging to capture the combustion temperature field's details. As a result, numerical simulations have received more attention. Moreover, most studies have focused on the effect of AP particle size and pressure on the burning rate, but little has been done on the content of fine AP [25–28]. In fact, AP content, especially fine AP content, has a significant effect. Experimental research shows that a 28% increase in the burning rate occurs as the amount of fine AP increases from 63 to 65 percent at 7 MPa [29]. Furthermore, coarse AP particles located at the edge of the propellant grain may be unevenly distributed during propellant casting, intensifying the propellant's burning rate edge effect. Consequently, this paper studies the effects of total and fine AP contents and the position of coarse AP on flame structure and burning rate based on the gas–solid-coupled AP/HTPB composite propellant sandwich combustion model.

2. Modeling

2.1. Geometry

The sandwich model of the propellant is displayed in Figure 1. In the figure, y = 0 μm denotes the burning surface, which defines the interface between the gas and solid phases. The solid-phase region below the surface contains AP and a binder matrix that is a homogeneous mixture of HTPB and fine AP. The widths of the coarse AP and binder matrix are calculated based on their respective contents. The propellant has a width of 100 μm and a height of 800 μm. Above the burning surface is the gas-phase region, which has the same computational domain as the solid-phase region.

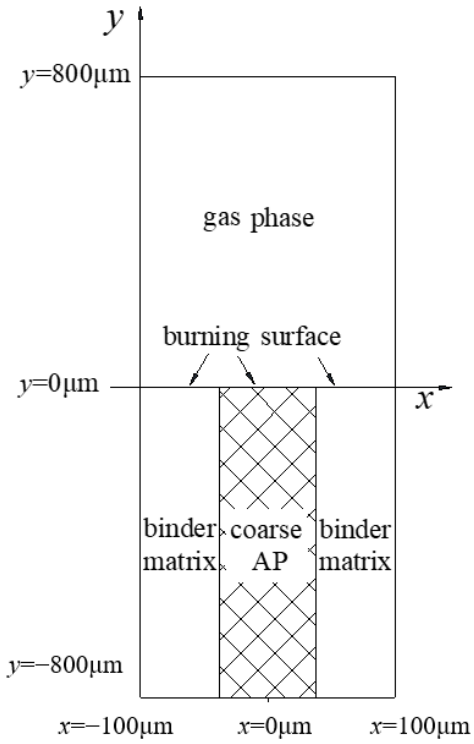

Figure 1. The geometry of the sandwich model.

2.2. Solid Phase

The thermal decomposition of AP and HTPB is considered a simple reaction that occurs in the thin layer of the solid-phase surface to simplify the model, and only simple heat conduction occurs in the remaining solid-phase region below the thin layer. Studies have shown that AP crystals typically undergo a phase transition from orthogonal to cubic structure at 513 K [11]. As the temperature continues to increase, the lattice becomes unstable and melts at approximately 725–825 K [30], followed by an exothermic reaction from AP dissociation, sublimation, and decomposition. Roughly 30% of AP undergoes sublimation and evaporation, which produces NH_3 and $HCLO_4$, while the remaining 70% decomposes on the surface, resulting in an exothermic condensed-phase reaction. The resulting product then undergoes a series of chain reactions to form a premixed flame. The overall process of the AP condensed-phase decomposition can be expressed as follows [31]:

$$AP \rightarrow 0.3(NH_3 + HClO_4) + 0.7(1.5H_2O + 1.25O_2 + HCl + 0.5\,N_2) \quad (1)$$

HTPB is supposed to release C_4H_6 in the gas phase, according to the following reaction [32–34]:

$$HTPB \rightarrow C_4H_6 \quad (2)$$

The decomposition rates of the condensed phase are defined by pyrolysis laws [18]:

$$\begin{cases} \dot{m}_{AP} = \rho_{AP} r_{AP} = A_{AP} \exp(-E_{AP}/R_u T_{s,AP}) \\ \dot{m}_{HTPB} = \rho_{HTPB} r_{HTPB} = A_{HTPB} \exp(-E_{HTPB}/R_u T_{s,HTPB}) \end{cases} \quad (3)$$

where T_s is the surface temperature, R_u is the universal gas constant, and ρ is the solid density. Both the pre-exponential term A and the activation energy E are empirical constants. The thermodynamic data of AP and HTPB are shown in Table 1, primarily derived from reference [19,32]. The burning rate of pure AP is measured at 3.3 mm/s and the surface temperature at 850 K for 2.07 MPa, according to reference [35,36]. Therefore, the parameters of AP are calibrated to match the measured data [37,38]. When HTPB is blended

with AP as a binder matrix, the density, ρ_m, and burning rate, r_m, can be obtained using Equations (4) and (5), respectively [39].

$$\rho_m = \frac{1}{\frac{\alpha}{\rho_{AP}} + \frac{1-\alpha}{\rho_{HTPB}}} \tag{4}$$

$$r_m = r_{AP}^{\alpha} r_{HTPB}^{1-\alpha} \tag{5}$$

where α is the mass fraction of fine AP in the binder matrix.

Table 1. The thermodynamic data of AP and HTPB.

Parameter	Value	Unit
ρ_{AP}	1950	kg/m^3
ρ_{HTPB}	920	kg/m^3
A_{AP}	2,827,500	kg/m^2s
A_{HTPB}	9531.2	kg/m^2s
E_{AP}	91,820	J/mol
E_{HTPB}	62,355	J/mol
λ_{AP}	0.21	W/mK
λ_{HTPB}	0.14	W/mK
$c_{p,AP}$	1602	J/kgK
$c_{p,HTPB}$	2900	J/kgK
$Q_{s,AP}$	−385	kJ/kg
$Q_{s,HTPB}$	−226	kJ/kg

The heat conduction equation in the solid-phase region needs to be solved:

$$c_p \rho \frac{\partial T}{\partial t} = \nabla \cdot (\lambda \nabla T) \tag{6}$$

where the values of c_p, ρ, and λ are assigned according to whether a point is located in the binder matrix or coarse AP. In order to simplify the model, the λ and c_p of the binder matrix are still calculated as the parameters of HTPB.

2.3. Gas Phase

2.3.1. Global Kinetic Model

As detailed data for chemical kinetics in flames are often not available at high pressures and are more complex and costly to obtain, this paper employs a simplified 12-species and three-step global mechanism, which can accurately describe the flame structure, the composition of products for the reactions is obtained using the chemical equilibrium code NASA SP273, the product species considered here constitute more than 95% of all the predicted species [32–34].

$$NH_3 + HClO_4 \rightarrow 1.5H_2O + 1.25O_2 + HCl + 0.5\,N_2 \tag{7}$$

$$\begin{aligned} &C_4H_6 + 4.4(NH_3 + HClO_4) \\ &\rightarrow 1.4CO + 2.6CO_2 + 0.7Cl + 3.7HCl + 0.65H_2 + \\ &8.9H_2O + 2.2N_2 + 0.8OH + 0.65O_2 \end{aligned} \tag{8}$$

$$\begin{aligned} &C_4H_6 + 4.4(1.5H_2O + 1.25O_2 + HCl + 0.5N_2) \\ &\rightarrow 1.4CO + 2.6CO_2 + 0.7Cl + 3.7HCl + 0.65H_2 + 8.9H_2O + 2.2N_2 + 0.8OH + \\ &0.65O_2 \end{aligned} \tag{9}$$

The reaction rates of the aforementioned reactions are determined by a pressure-dependent Arrhenius equation expressed as [40]:

$$\dot{\omega} = A_g P^n \exp(-\frac{E_g}{R_u T}) \prod_{i=1}^{reac\tan ts} [Y_i] \tag{10}$$

where A_g, E_g, and n are a pre-exponential factor, activation energy, and pressure exponent, respectively, which are chosen so that the burning rates of the AP/HTPB propellant match the experimental results listed in Table 2.

Table 2. Parameters of the gas reactions.

Parameters	Equation (7)	Equation (8)	Equation (9)	Unit
A_g	1.89×10^7	1.5×10^7	1.5×10^7	$kmol/(m^3 \cdot s \cdot bar^n)$
n	1.4	1	1.4	-
E_g	6.77×10^4	4×10^4	6×10^4	J/mol

2.3.2. Governing Equations

The governing equations for the gas phase describe the conservation of mass, chemical species, momentum, and energy.

$$\frac{\partial \rho_g}{\partial t} + \vec{\nabla} \cdot (\rho_g \vec{v}) = S_{\text{mass}} \tag{11}$$

$$\frac{\partial \rho_g \vec{v}}{\partial t} + \vec{\nabla} \cdot (\rho_g \vec{v} \vec{v}) = -\vec{\nabla} p + \vec{\nabla} \bar{\bar{\tau}} + S_{\text{momentum}} \tag{12}$$

$$\frac{\partial \rho_g E}{\partial t} + \vec{\nabla} \cdot (\vec{v}(\rho_g E + p)) = \vec{\nabla} \cdot (k_{\text{eff}} \nabla T - \sum_{k=1}^{N} h_k \vec{J}_k + \bar{\bar{\tau}} \cdot \vec{v}) + S_{\text{energy}} \tag{13}$$

$$\frac{\partial \rho_g Y_k}{\partial t} + \vec{\nabla} \cdot (\rho_g \vec{v} Y_k) = -\vec{\nabla} \cdot \vec{j}_k + W_k \dot{\omega}_k + S_{species} \tag{14}$$

where ρ_g is the density of gas, $\vec{v}$ is the velocity vector, Y_k is the mass fraction of the species k, $\vec{j}_k$ is the diffusion flux of species k, h_k is the enthalpy of species k per mass unit, W_k is the molar weight of species k, $\dot{\omega}_k$ is the molar reaction rate of species k, p is the pressure, $\bar{\bar{\tau}}$ is the stress tensor, and E is the total energy.

2.4. Boundary Condition

The temperature and normal mass fluxes are continuous across the surface. In this model, the gas-phase components are assumed to be formed in a very thin region adjacent to the burning surface; therefore, the adjacent gas-phase grid will be taken as an added-mass cell, and propellant gas will be added into the flow field simulation as source terms of the gas-phase Equations (11)–(14). The details of those source terms are as follows:

$$\begin{bmatrix} S_{\text{mass}} \\ S_{\text{momentum}} \\ S_{\text{energy}} \\ S_{\text{species}} \end{bmatrix} = \begin{bmatrix} \dot{m}/\Delta y \\ \dot{m}v/\Delta y \\ \dot{m}Q_s/\Delta y \\ \dot{m}Y_i/\Delta y \end{bmatrix} \tag{15}$$

where Δy is the height of the grid cell near the burning surface, v is the velocity of gas-phase products, and can be calculated by the mass conservation as $v = \rho r/\rho_g$ where Q_s is the reaction heat of the solid phase. The corresponding pressure and temperature are used at the exit plane. The bottom plane is set to a wall of 300 K. The temperature of the gas phase is 1400 K to initialize the ignition, and the initial species filling in the gas zone is N_2.

2.5. Verification

Numerical simulation is performed and compared with the experimental data to verify the ability and accuracy of the present model in capturing the process of AP/HTPB combustion. The experimental burning rate of propellant SD III-17 presented by Miller [26] is employed to compare with the result obtained by the present model. The 20 μm AP is treated as the fine AP in the model. As shown in Figure 2, the burning rates r are in good agreement with the experiment, with an average error of 5% for all points. In conclusion, the applied numerical simulation yields satisfying results so that the combustion model can be used in the current study.

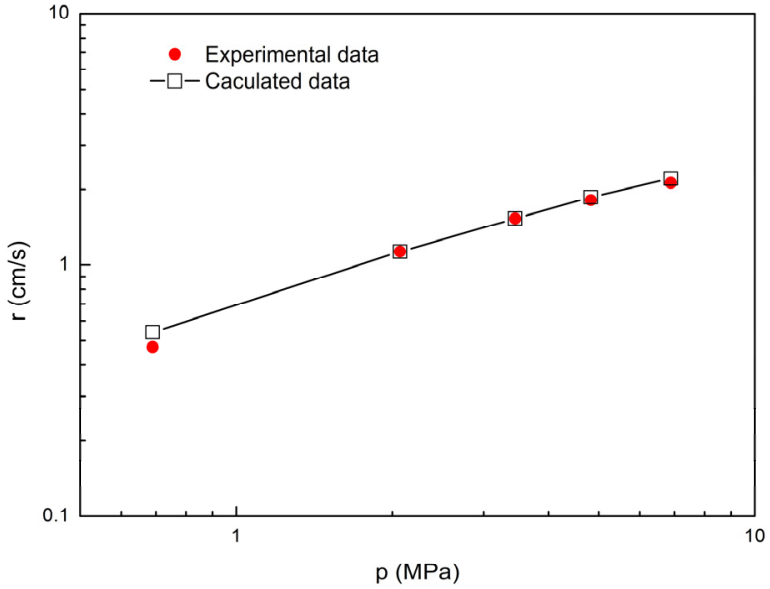

Figure 2. Comparison of experiment with computation.

3. Results and Discussion

3.1. Effect of Total AP Content

Propellants with various mass fractions of total AP are studied. The total AP mass fraction ranges from 70% to 95%, where the ratio of coarse and fine AP remains constant at 0.57:1. Three of the propellants' geometry is shown in Figure 3. As the AP mass fraction increases, the region occupied by coarse AP gradually expands.

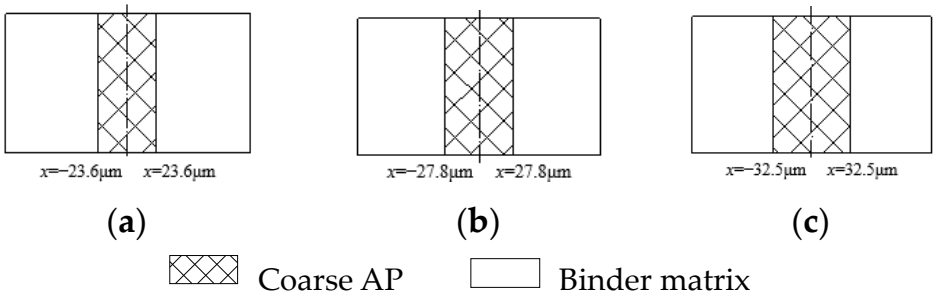

Figure 3. Three propellants with different mass fractions of total AP: (**a**) 80% AP; (**b**) 87.5% AP; (**c**) 95% AP.

Figure 4 shows the temperature field for three of the propellants at 6.89 MPa, with maximum temperatures of 2930 K, 3040 K, and 2700 K and average temperatures corresponding to 2529 K, 2859 K, and 2471 K for each. Furthermore, the adiabatic combustion temperature of the combustion at pressures of 6.89 MPa was calculated by chemical equilibrium application (CEA) code and compared with the present predictions. The maximum error is 7%. The variation of the burning rate and surface temperature of the propellant

with total AP content is shown in Figure 5. The burning rate initially increases and then decreases with the total AP content. The highest burn rate of 2.3 cm/s is achieved at an AP content of 87.5%, with a similar trend for the surface temperature. It indicates that the overall oxygen-to-fuel ratio of the propellant has a significant effect on the gas-phase flame temperature and burn rate. In addition, there exists an optimal oxygen-to-fuel ratio that maximizes the burning rate, as found in reference [41]. Therefore, a propellant containing 87.5% AP is selected for the follow-up study.

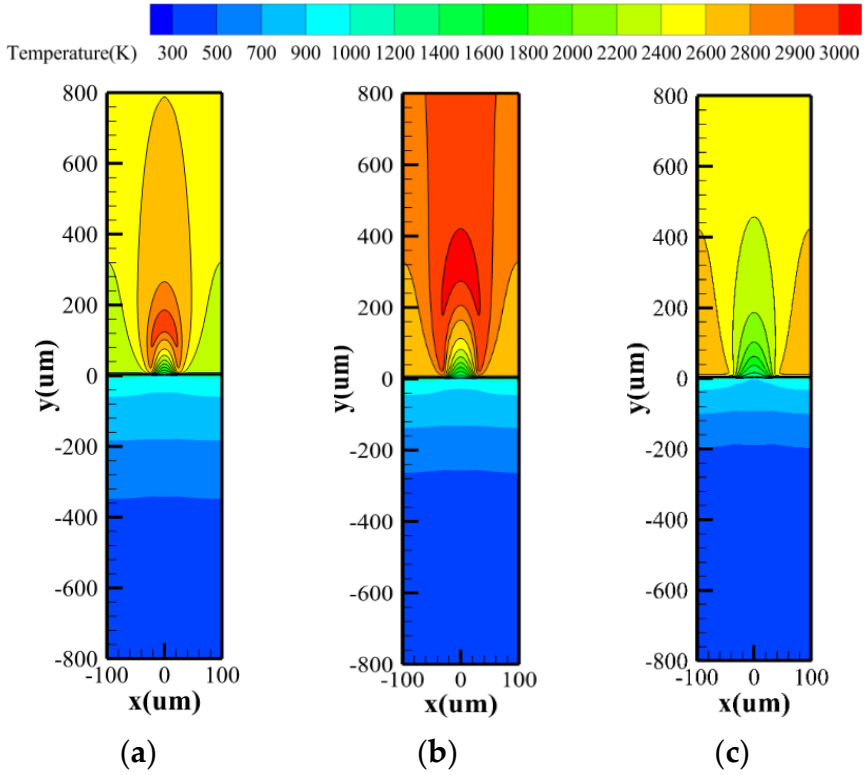

Figure 4. Gas-phase and solid-phase temperature distribution with different mass fractions of total AP: (**a**) 80% AP; (**b**) 87.5% AP; (**c**) 95% AP.

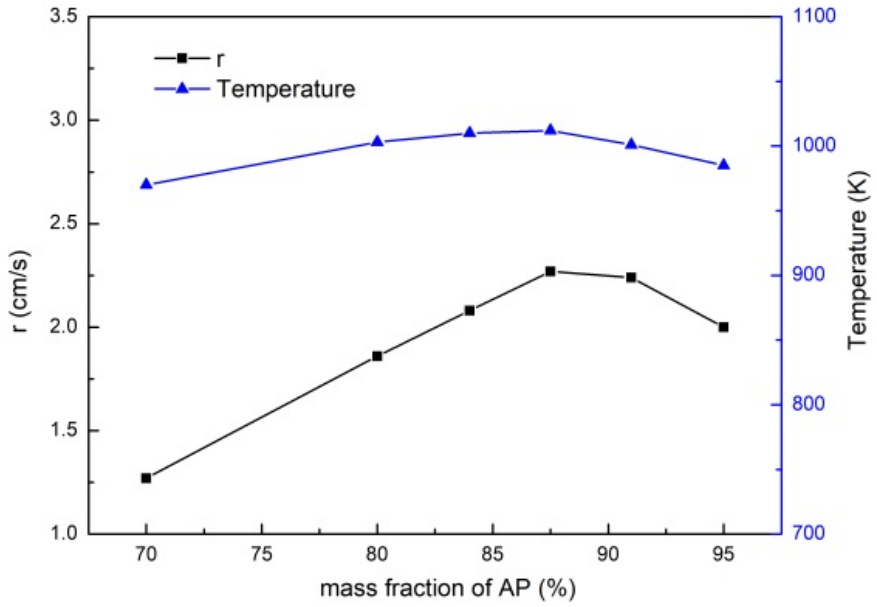

Figure 5. The change of burning rate with mass fractions of total AP.

3.2. Effect of Fine AP Content

Four propellants are selected in this section to study the effect of fine AP content with varying mass fractions, as shown in Table 3. The propellants P-1 to P-4 are prepared with different levels of fine AP, ranging from 0% to 70%. When the mass fraction of fine AP increased while the content of HTPB remained constant, some coarse AP was replaced by fine AP. This results in a decrease in the width of coarse AP and an increase in the width of the binder matrix, as illustrated in Figure 6.

Table 3. Propellant formulations with different fine AP contents.

Propellant	Mass Fraction of AP (%)		Mass Fraction of HTPB (%)
	90 μm	20 μm	
P-1	87.5	0	12.5
P-2	59.0	28.5	
P-3	31.6	55.9	
P-4	17.5	70.0	

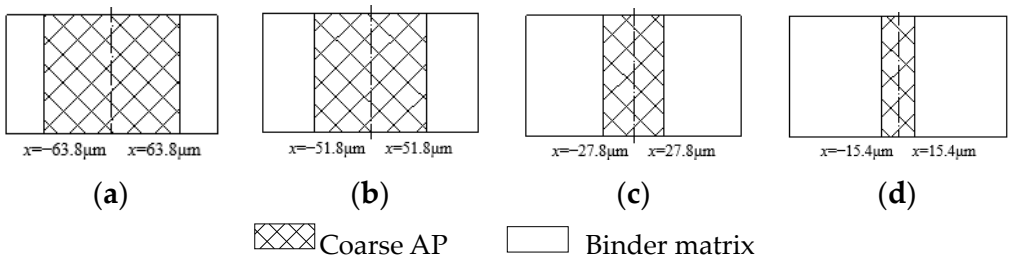

Figure 6. Four propellants with different mass fractions of fine AP: (**a**) P-1; (**b**) P-2; (**c**) P-3; (**d**) P-4.

The temperature field is used to describe the overall flame structure. The results in Figure 7 indicate that, at a pressure of 6.89 MPa, the flame structure of P-2 exhibited a multi-flame structure, which is consistent with the findings observed in the experimental results [15] as well as the improved BDP model [24]. This suggests that the numerical simulation method adopted in this study is reliable and can effectively predict the flame structure of the propellant system. The AP decomposition flame mainly dominates the combustion of coarse AP particles on its surface. The primary diffusion flame is located near the burning surface at the AP/HTPB interface, while the final one is situated above it. Moreover, the premixed binder flame is formed above the binder matrix as a result of the reaction between decomposed AP and HTPB that are homogeneously mixed.

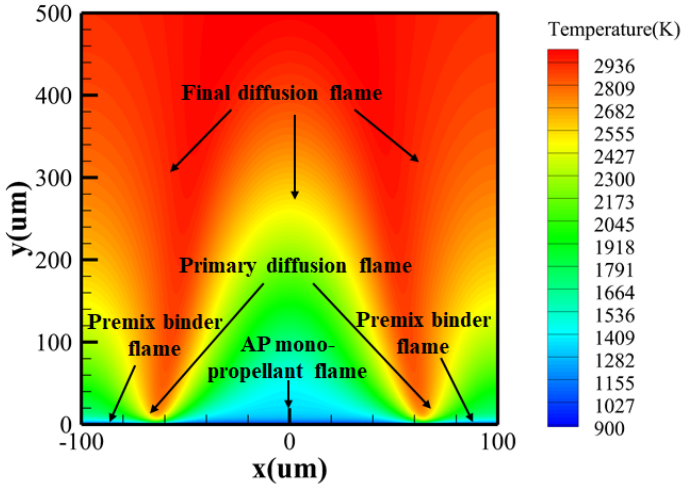

Figure 7. Flame structure of P-2 at 6.89 MPa.

Figure 8 shows the results of combustion simulation at 6.89 MPa for the four propellants listed in Table 3, all of which reached temperatures of 3000 K. Although the temperature distribution of the four propellants in the gas phase is quite different, the solid phase is basically the same, which is due to only heat conduction in the solid phase. The flame shape above the binder matrix is closely related to the fine AP content. When there is an increase in fine AP content, the premixed flame above the binder matrix gradually dominates over the diffusion flame (see Figure 8a–d), resulting in significant improvements in the thermal feedback of the flame to the burning surface. Furthermore, the diffusion flame also changes. The highest temperature region above the binder matrix in our experiment reached 3000 K, and this region is relatively small, as shown in Figure 8a. With an increase in the fine AP content, the high-temperature region shifted to the top of the coarse AP (as seen in Figure 8b). As Figure 8c shows, when the mass fraction of fine AP reaches 55.9%, the leading edge of the diffusion flame approaches the burning surface. When the amount of fine AP is further increased (as seen in Figure 8d), the high-temperature region becomes larger and closer to the surface. The average temperatures in the gas-phase regions for all four propellants tested in our research were 2562 K, 2749 K, 2859 K, and 2950 K, respectively. Heat feedback from the diffusion flame to the burning surface is determined by the heat release of the flame and the distance between the leading edge and the burning surface. As the mass fraction of fine AP increases, Figure 8d demonstrates that the heat feedback of the diffusion flame to the burning surface increases while the distance decreases, resulting in a significant increase in the burning rate. The heat feedback from the diffusion flame to the burning surface is affected by both the heat release of the flame and the distance between the leading edge and the burning surface. Figure 8 shows that an increase in the mass fraction of fine AP leads to greater heat release to the burning surface and a decrease in the distance between them. This greatly increases the heat feedback to the surface, which significantly increases the burning rate.

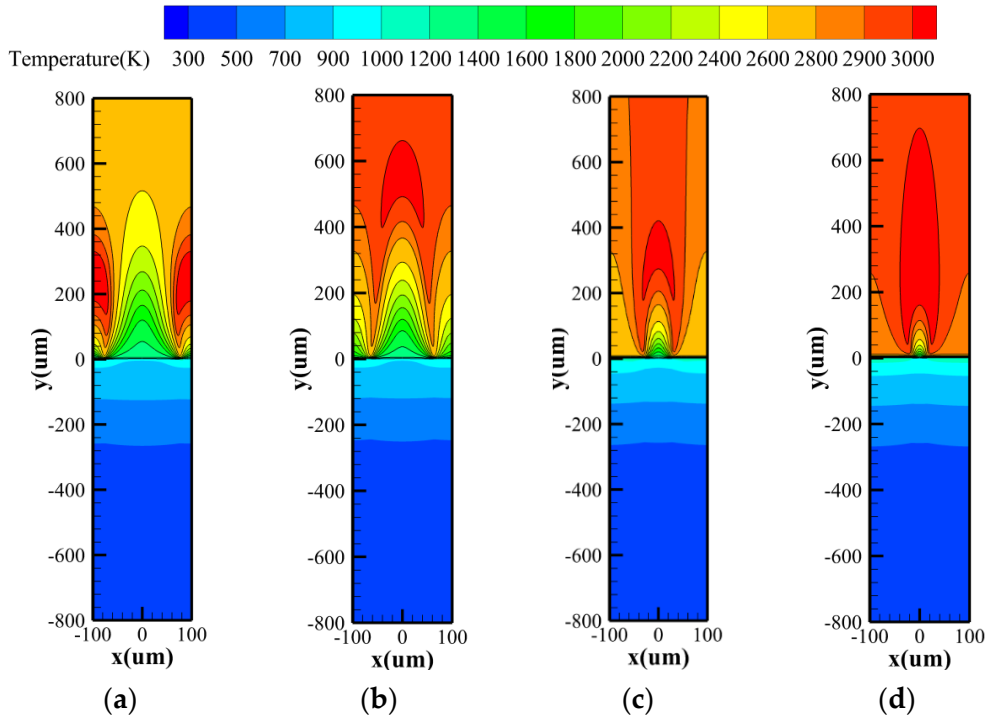

Figure 8. Gas-phase and solid-phase temperature distribution with different fine AP: (**a**) P-1; (**b**) P-2; (**c**) P-3; (**d**) P-4.

Figure 9 displays the temperature profile along the y-axis at x = 0 μm (coarse AP central location) and x = ±100 μm (binder matrix central location). As shown in Figure 9a, P-1 reaches a maximum temperature of 2600 K in the gas-phase region with the smallest

temperature gradient, while P-4 reaches 3000 K with the largest gradient. This indicates that the heat feedback of the diffusion flame is enhanced with an increasing mass fraction of fine AP. Figure 9b illustrates the temperature gradient variation above the binder matrix. For P-1, the high-temperature region is above the binder matrix, and the temperature reaches 3000 K. As for P-2, the diffusion flame is still dominant above the binder matrix when the high-temperature region transfers to above the coarse AP, and both the temperature and gradient decrease. In contrast, when the premixed flame replaces the diffusion flame as the dominant factor, as shown in P-3 and P-4, the gradient increases significantly.

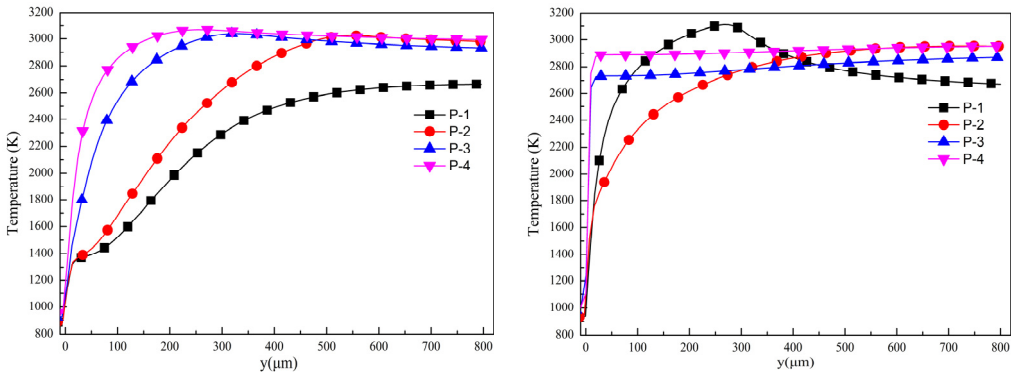

Figure 9. The distribution of temperature along the y-axis at different positions: (**a**) x = 0 μm; (**b**) x = ±100 μm.

The average surface temperature and burning rate for the four propellants are presented in Figure 10. As the mass fraction of fine AP increases from 0% to 70.0%, the surface temperature increases from 937 K to 1026 K, and the burning rate rises from 0.9 cm/s to 2.7 cm/s.

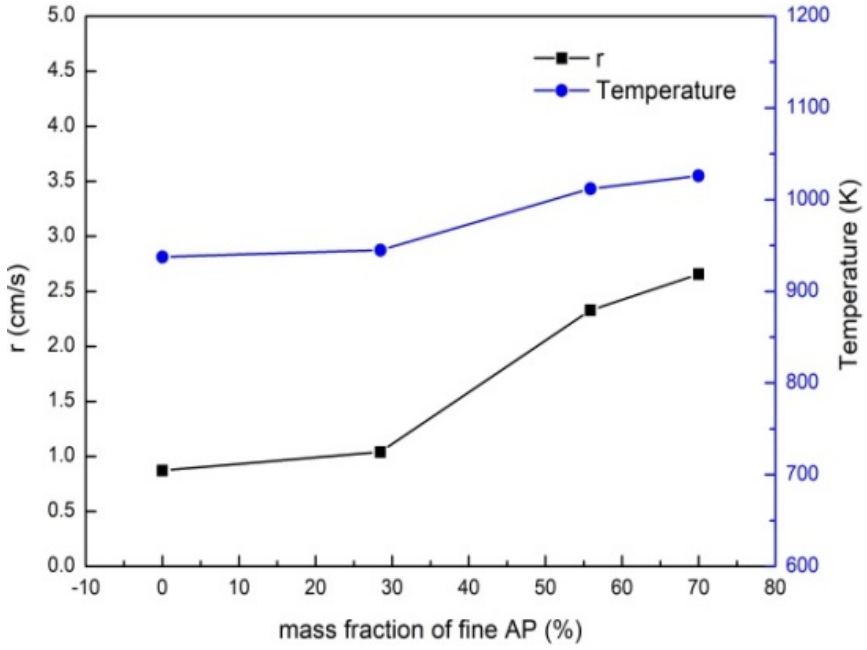

Figure 10. The change of burning rate with the content of fine AP.

Figures 11 and 12 display the mass fraction distribution of the reactant C_4H_6 and the product CO. For P-1 in Figure 11a, the binder matrix lacks fine AP. As a result, C_4H_6 is diffusively mixed with the decomposition products of AP and the combustion products of the AP decomposition flame to complete combustion near the interface between AP

and HTPB. The farther away from the surface, the less C_4H_6 is left, and the more CO is produced (Figure 12a). As the mass fraction of fine AP increases, the decomposition products of fine AP and HTPB react quickly on the surface of the binder matrix. Most of the C_4H_6 is consumed near the surface, and the rest is consumed by the diffusion flame far away. Compared with Figure 11a,b, the maximum mass fraction of C_4H_6 is reduced from 0.6 to 0.2 in Figure 11c,d. The distribution law for the CO products in Figure 12 is the exact opposite, with a large increase in the CO mass fraction.

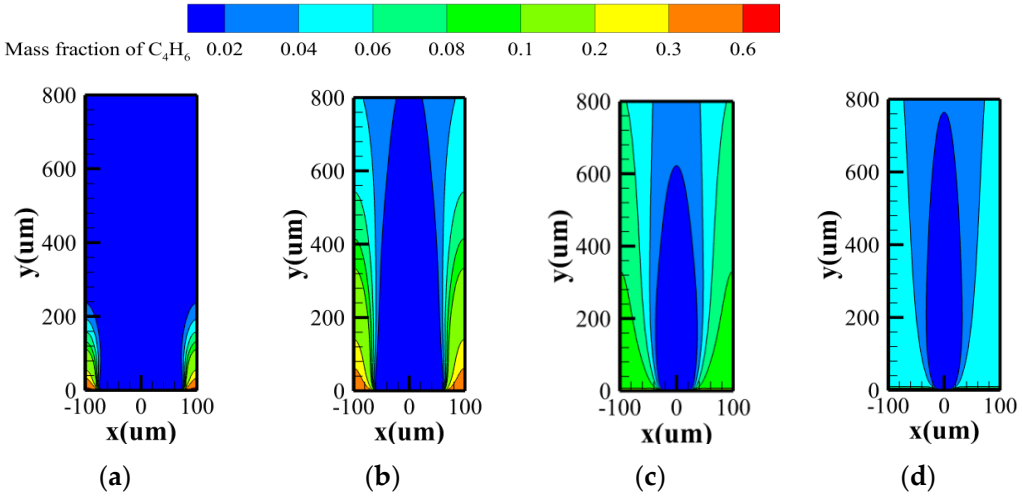

Figure 11. The mass fraction distribution of C_4H_6: (**a**) P-1; (**b**) P-2; (**c**) P-3; (**d**) P-4.

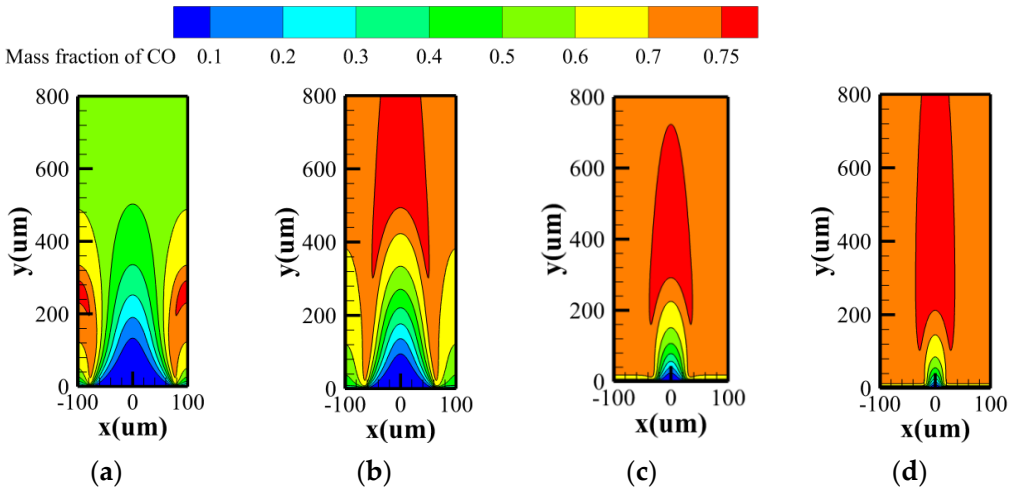

Figure 12. The mass fraction distribution of CO: (**a**) P-1; (**b**) P-2; (**c**) P-3; (**d**) P-4.

3.3. Effect of Coarse AP Position

This section investigates the effect of the non-uniform distribution of coarse AP on the burning rate and flame structure by shifting the location of the coarse AP. To achieve this, the coarse AP of P-3 (Figure 13a) is shifted to the right by 20 μm, 40 μm, and 60 μm, respectively, resulting in Figure 13b–d.

Figure 14 shows the temperature distributions for different coarse AP positions with the same propellant formulation. It is obvious that the temperature distribution is no longer symmetric in both the solid and the gas-phase regions. The center of the flame shifts with the coarse AP offset, and the high-temperature region of the diffusion flame gradually tilts to the side with less binder matrix. This trend suggests that if two coarse AP particles are close enough, their respective flames will bend towards each other, resulting in the merging of the flames. Additionally, the average gas-phase temperatures are 2859 K, 2860 K, 2865 K,

and 2826 K, respectively. The distance between the leading edge of the diffusion flame and the burning surface does not change significantly, indicating that the heat feedback from the diffusion flame to the surface is relatively unchanged.

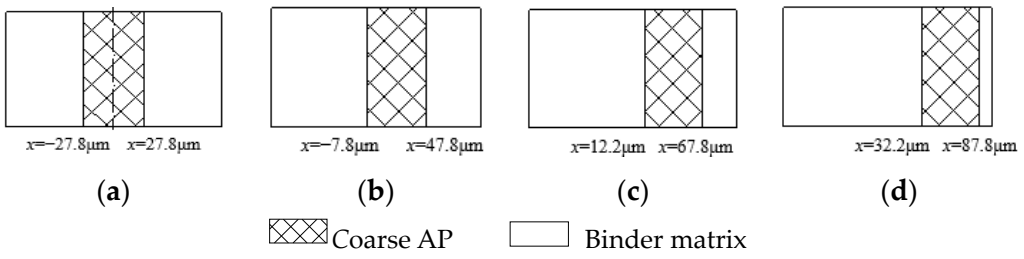

Figure 13. Different positions of the coarse AP with the same propellant formulation: (**a**) P-3; (**b**) P-3-1; (**c**) P-3-2; (**d**) P-3-3.

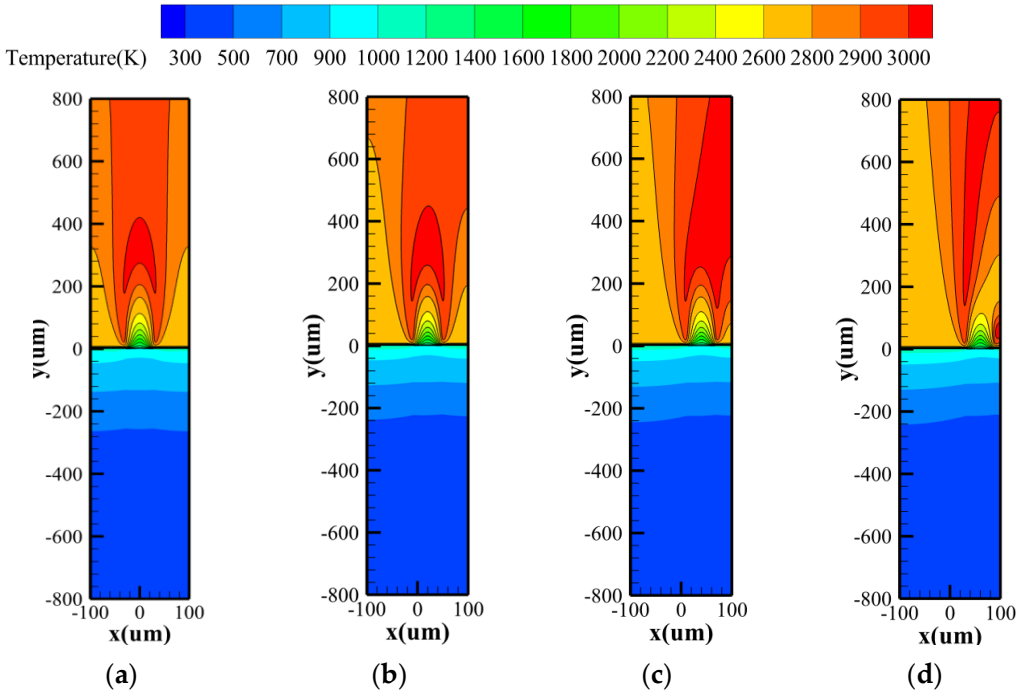

Figure 14. Temperature distribution for different coarse AP positions with the same propellant formulation: (**a**) P-3; (**b**) P-3-1; (**c**) P-3-2; (**d**) P-3-3.

The temperature distribution along the *y*-axis is studied at the position of the coarse AP center (x = 0 μm for P-3, x = 20 μm for P-3-1, x = 40 μm for P-3-2, and x = 60 μm for P-3-3) and x = 100 μm, as shown in Figure 15. With the increase of the offset distance of the coarse AP, the temperature in the gas phase shows little variation until the distance reaches 60 μm, of which the temperature difference becomes obvious (see Figure 15a). Figure 15b shows that the temperature at $x = -100$ μm decreases with increasing distance, while Figure 15c shows the opposite trend except for the P-3-3, where the diffusion flame structure is incomplete due to bending. The surface temperature and burn rate of the propellants remain essentially unchanged at 1011 K and 2.3 cm/s, respectively. This is because the values are calculated as averages over all burning surfaces, which compensates for any left–right differences. The fundamental reason is that the mass fraction of the fine AP is constant, and the heat feedback from the diffusion and premixed binder flames are invariant.

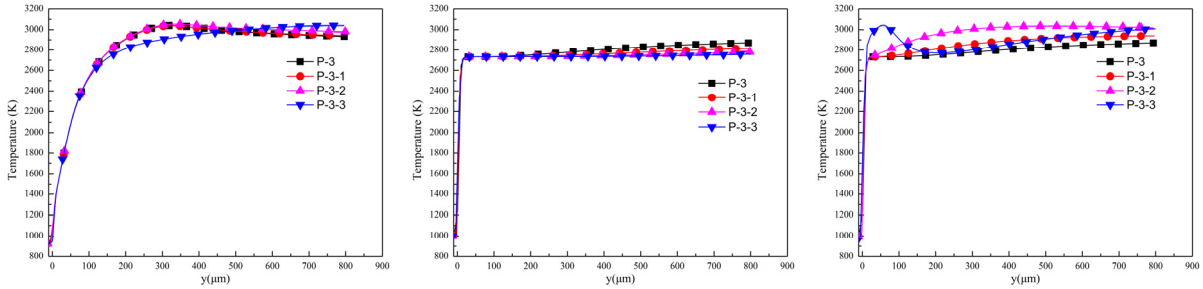

Figure 15. The distribution of temperature along the *y*-axis at different positions: (**a**) the center of coarse AP (**b**) $x = -100$ μm; (**c**) $x = 100$ μm.

Figures 16 and 17 show the mass fraction distribution of C_4H_6 and CO; as the coarse AP offset distance increases, the mass fraction distribution of reactants and products becomes asymmetric. Notably, there is no significant change in the mass fraction distribution near the burning surface. This indicates that only the diffusion flame changes, while the premixed binder flame remains unaffected.

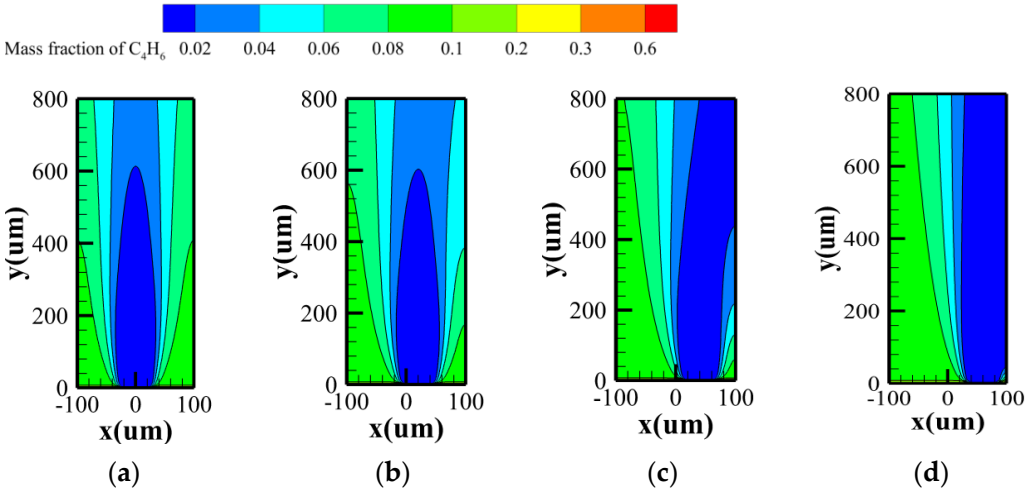

Figure 16. The mass fraction distribution of C_4H_6: (**a**) P-3; (**b**) P-3-1; (**c**) P-3-2; (**d**) P-3-3.

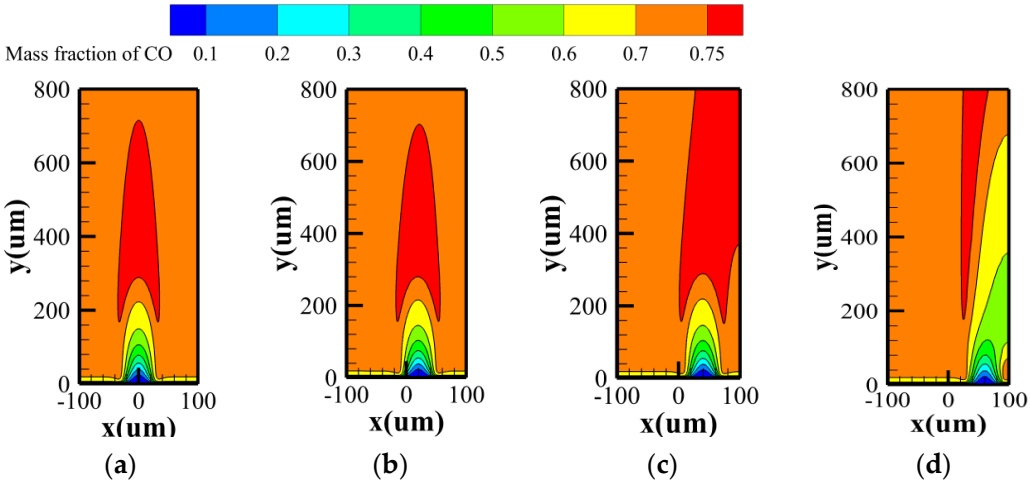

Figure 17. The mass fraction distribution of CO: (**a**) P-3; (**b**) P-3-1; (**c**) P-3-2; (**d**) P-3-3.

4. Conclusions

(1) A gas-phase and solid-phase-coupled sandwich combustion model is constructed in this paper and compared with the experimental results. The model exhibited high precision, with an average error in burning rates within 5%;
(2) The temperature of the gas phase and burning rate initially increases and then decreases with the overall AP content; there is an optimal oxygen-to-fuel ratio that maximizes the burning rate, which is nearly 87.5%;
(3) With the increase of fine AP mass fraction, the diffusion flame gradually loses its dominance over the premixed flame above the binder matrix. Additionally, the diffusion flame near the interface of coarse AP and binder matrix grows stronger, getting closer to the burning surface, creating stronger thermal feedback and increasing the burning rate. As the mass fraction of fine AP increases from 0% to 70.0%, the average surface temperature rises from 937 K to 1026 K, and the combustion rate increases from 0.9 cm/s to 2.7 cm/s;
(4) Despite the asymmetry caused by the location of the coarse AP, the average temperature and burning rate are not significantly affected, remaining at 1011 K and 2.3 cm/s, respectively. This implies that the asymmetry diffusion flame has little impact on the burning rate.

Author Contributions: D.S.: methodology, software, validation, formal analysis, investigation, visualization, writing—original draft. Y.L.: conceptualization, software, validation, visualization, writing—review and editing. P.L.: conceptualization, supervision, funding acquisition. B.C.: validation and visualization. W.F.: review and editing. All authors have read and agreed to the published version of the manuscript.

Funding: This research was funded by the Open Fund for the Key Laboratory of Science and Technology on Combustion, Internal Flow, and Thermal-Structure Laboratory (No. GT202206139); the Science and Technology Project of Education Department of Jiangxi Province (No. DA202206129); the Jiangxi Province Innovation Leading Talent Project (No. CK202206068).

Data Availability Statement: The datasets generated or analyzed during this study are available from the corresponding author upon reasonable request.

Conflicts of Interest: The authors declare there are no conflicts of interest regarding the publication of this paper.

Nomenclature

A	Arrhenius pre-exponential factor for solid propellant pyrolysis, kg/m^{2}s
A_g	Arrhenius pre-exponential factor for gas-phase reactions, kmol/(m^3·s·bar^n)
n	pressure exponents in the reaction rates
$\dot{m}$	mass flow rate, kg/s
R_u	universal gas constant
c_p	specific heat, J/kg·K
Q_s	reaction heat of the solid, kJ/kg
p	pressure, bar
S	source term in the generalized equation
r	burning rate, mm/s
E	Arrhenius activation energy, J/mol
Y_k	mass fraction of species, k
ρ	density, kg/m^3
T	temperature, K
α	mass fraction of fine AP in the binder matrix
λ	heat conductivity, W/m.K
ν	velocity of gas-phase products, mm/s

Subscripts

AP	ammonium perchlorate
HTPB	hydroxyl-terminated polybutadiene

s	surface
g	gas-phase
m	fine AP/HTPB binder matrix

References

1. Mini, S.; Ponti, F.; Brusa, A.; Bertacin, R.; Betti, B. Prediction of tail-off pressure peak anomaly on small-scale rocket motors. *Aerospace* **2023**, *10*, 169. [CrossRef]
2. Hernandez, R.; Singh, H.; Messimer, S.; Patterson, A. Design and performance of modular 3-D printed solid-propellant rocket airframes. *Aerospace* **2017**, *4*, 17. [CrossRef]
3. Dennis, C.; Bojko, B. On the combustion of heterogeneous AP/HTPB composite propellants: A review. *Fuel* **2019**, *254*, 115646. [CrossRef]
4. Yue, S.; Liu, L.; Liu, H.; Jiang, Y.; Liu, P.; Pang, A.; Zhang, G.; Ao, W. Agglomerate size evolution in solid propellant combustion under high pressure. *Aerospace* **2023**, *10*, 515. [CrossRef]
5. Orlandi, O.; Plaud, M.; Godfroy, F.; Larrieu, S.; Cesco, N. Aluminium droplets combustion and SRM instabilities. *Acta Astronaut.* **2019**, *158*, 470–479. [CrossRef]
6. Liu, X.; Hu, S.; Liu, L.; Zhang, Y. Condensed combustion products characteristics of HTPB/AP/AL propellants under solid rocket motor conditions. *Aerospace* **2022**, *9*, 677. [CrossRef]
7. Elbasuney, S.; Fahd, A.; Mostafa, H. Combustion characteristics of extruded double base propellant based on ammonium perchlorate/aluminum binary mixture. *Fuel* **2017**, *208*, 296–304. [CrossRef]
8. Mullen, J.; Brewster, M. Reduced agglomeration of aluminum in wide-distribution composite propellants. *J. Propuls. Power* **2011**, *27*, 650–661. [CrossRef]
9. Cohen, N.; Strand, L. An improved model for the combustion of AP composite propellants. *AIAA J.* **2012**, *20*, 1739–1746. [CrossRef]
10. Cohen, N. Review of composite propellant burn rate modeling. *AIAA J.* **1979**, *18*, 277–293. [CrossRef]
11. Price, C.; Boggs, T.; Derr, R. Modeling of solid monopropellant deflagration. In Proceedings of the AIAA 16th Aerospace Sciences Meeting, Huntsville, Alabama, 16–18 January 1978.
12. Glick, R. On statistical analysis of composite solid propellant combustion. *AIAA J.* **1949**, *12*, 384–385. [CrossRef]
13. Beckstead, M.; Derr, R.; Price, C. A model of composite solid-propellant combustion based on multiple flames. *AIAA J.* **1970**, *8*, 2200–2207. [CrossRef]
14. Jeppson, M.; Beckstead, M.; Jing, Q. A kinetic model for the premixed combustion of a fine AP/HTPB composite propellant. In Proceedings of the AIAA Aerospace Sciences Meeting and Exhibit, Reno, NV, USA, 12–15 January 1998.
15. Chorpening, B.; Knott, G.; Brewster, M. Flame structure and burning rate of ammonium perchlorate/hydroxyl-terminated polybutadiene propellant sandwiches. *Proc. Combust. Inst.* **2000**, *28*, 847–853. [CrossRef]
16. Chorpening, B.; Brewster, M. Emission imaging of AP/HTPB propellant sandwich combustion. *Combust. Sci. Technol.* **2002**, *174*, 39–60. [CrossRef]
17. Knott, G.; Jackson, T.; Buckmaster, J. Random Packing of Heterogeneous Propellants. *AIAA J.* **2001**, *39*, 678–686. [CrossRef]
18. Massa, L.; Jackson, T.; Short, M. Numerical solution of three-dimensional heterogeneous solid propellants. *Combust. Theory Model.* **2003**, *7*, 579–602. [CrossRef]
19. Jackson, T.; Buckmaster, J. Heterogeneous propellant combustion. *AIAA J.* **2002**, *40*, 1122–1130. [CrossRef]
20. Price, E.; Sambamurthi, J.; Sigman, R.; Panyam, R. Combustion of ammonium perchlorate-polymer sandwiches. *Combust. Flame* **1986**, *63*, 381–413. [CrossRef]
21. Fitzgerald, R.; Brewster, M. Flame and surface structure of laminate propellants with coarse and fine ammonium perchlorate. *Combust. Flame* **2004**, *136*, 313–326. [CrossRef]
22. Buckmaster, J.; Jackson, T.; Yao, J. An elementary discussion of propellant flame geometry. *Combust. Flame* **1999**, *117*, 541–552. [CrossRef]
23. Hegab, A.; Jacson, L.; Buckmaster, J.; Stewart, D. Nonsteady burning of periodic sandwich propellants with complete coupling between the solid and gas phases. *Combust. Flame* **2001**, *125*, 1055–1070. [CrossRef]
24. Gross, M.; Beckstead, M. Diffusion flame calculations for composite propellants predicting particle-size effects. *Combust. Flame* **2010**, *157*, 864–873. [CrossRef]
25. Jain, S.; Mehilal, M.; Nandagopal, S.; Singh, P.P.; Radhakrishnan, K.K.; Bhattacharya, B. Size and Shape of Ammonium Perchlorate and their Influence on Properties of Composite Propellant. *Def. Sci. J.* **2009**, *59*, 294–299. [CrossRef]
26. Miller, R. Effects of particle size on reduced smoke propellant ballistics. In Proceedings of the 18th Joint Propulsion Conference, Cleveland, OH, USA, 21–23 June 1982.
27. Renie, J.; Condon, J.; Osborn, J. Oxidizer size distribution effects on propellant combustion. *AIAA J.* **2015**, *17*, 877–883. [CrossRef]
28. Fong, C.; Smith, R. The relationship between plateau burning behavior and ammonium perchlorate particle size in HTPB-AP composite propellants. *Combust. Flame* **1987**, *67*, 235–247. [CrossRef]
29. Kohga, M. Burning rate characteristics of ammonium perchlorate-based composite propellant using bimodal ammonium perchlorate. *J. Propuls. Power* **2008**, *24*, 499–506. [CrossRef]

30. Guirao, C.; Williams, F. A model for ammonium perchlorate deflagration between 20 and 100 atm. *AIAA J.* **1971**, *9*, 1345–1356. [CrossRef]
31. Ramakrishna, P.; Paul, P.; Mukunda, H. Sandwich propellant combustion: Modeling and experimental comparison. *Proc. Combust. Inst.* **2002**, *29*, 2963–2973. [CrossRef]
32. Gaduparthi, T.; Pandey, M.; Chakravarthy, S. Gas phase flame structure of solid propellant sandwiches with different reaction mechanisms. *Combust. Flame* **2016**, *164*, 10–21. [CrossRef]
33. Chidambaram, P.K.; Kumar, A. A numerical investigation of oxidizer mixed hybrid rocket motors. *Aerosp. Sci. Technol.* **2015**, *45*, 10–16. [CrossRef]
34. Zou, X.; Wang, N.; Wang, C.; Wang, J.; Tang, Y.; Shi, B. Investigation on the microscale combustion characteristics of AP/HTPB propellant under wide pressure range. *Fuel* **2021**, *306*, 121652. [CrossRef]
35. Beckstead, M.; Hightower, J. Surface temperature of deflagrating ammonium perchlorate crystals. *AIAA J.* **1967**, *5*, 1785–1790. [CrossRef]
36. Mitani, T.; Niioka, T. Double Flame Structure in AP Combustion. *Symp. (Int.) Combust.* **1985**, *20*, 2043–2049. [CrossRef]
37. Ramakrishna, P.; Paull, P.; Mukunda, H. Revisiting the Modeling of Ammonium Perchlorate Combustion: Development of an Unsteady Model. *J. Propuls. Power* **2015**, *22*, 661–668. [CrossRef]
38. Rasmussen, B.; Frederick, J. A nonlinear heterogeneous model of composite solid propellant combustion. *J. Propuls. Power* **2002**, *18*, 1086–1092. [CrossRef]
39. Chen, M.; Buckmaster, J.; Jackson, T.; Massa, L. Homogenization issues and the combustion of heterogeneous solid propellants. *Proc. Combust. Inst.* **2002**, *29*, 2923–2929. [CrossRef]
40. Gross, M.; Hedman, T.; Son, S.; Jackson, T.; Beckstead, M. Coupling micro and meso-scale combustion models of AP/HTPB propellants. *Combust. Flame* **2013**, *160*, 982–992. [CrossRef]
41. Massa, L.; Buckmaster, J.; Jackson, T.L. New kinetics for a model of heterogeneous propellant combustion. *J. Propuls. Power* **2005**, *15*, 654–660. [CrossRef]